1874-8422/20 *Send Orders for Reprints to reprints@benthamscience.net*

44

Open Chemistry Journal

Content list available at: https://openchemistryjournal.com

RESEARCH ARTICLE

Sol-gel Autocombustion Elaboration and Physiochemical Characterizations of Cu^{2+} Substituted Cobalt Ferrite Nanoparticles

N. Hamdi[1], L. Bessais[2] and W. Belam[1,*]

[1]*Laboratory of Resources, Materials and Ecosystem, Bizerta Science Faculty, Carthage University, 7021 Jarzouna, Bizerta, Tunisia*
[2]*Université Paris Est, 2-8 rue Henri Dunant, F-94320 Thiais, France*

Abstract:

Introduction:

The copper doped cobalt ferrite series, with nominal formula $Cu_XCo_{1-X}Fe_2O_4$ (X = 0, 0.25, 0.5, 0.75, 1), has been elaborated *via* sol-gel autocombustion process by copper substitution procedure into cobalt ferrite framework.

Methods:

The five synthesized ferrites have been analyzed by X-ray powder diffraction, Fourier transform infrared spectroscopy, field emission scanning electron microscopy coupled to energy dispersive X-ray spectroscopy, complex impedance spectroscopy and superconducting quantum interference device magnetometry.

Results and Discussion:

The analysis of the results allowed to deduce that the cubic spinel basic structure was not modified by the incorporation of copper into the host lattice and the corresponding pure fine powders obtained formed by homogeneous nanoparticles. The highest electrical conductivity value, $\sigma DC(373K) = 27.03x10^{-3}S.cm^{-1}$, was observed in the case of $CuFe_2O_4$.

Conclusion:

Moreover, the superparamagnetic behavior at room temperature has been confirmed by using both ZFC-FC and hysteresis magnetic measurement modes. In addition, the remarkable electrical conductivity and magnetic properties of the five explored nanoferrites, derived from the present investigation, enabled them useful in several modern nanotechnological and biomedical applications.

Keywords: Sol-gel, autocombustion, nanoferrite, X-ray powder diffraction, FESEM, impedance spectroscopy, magnetic properties.

Article History	Received: July 10, 2020	Revised: September 21, 2020	Accepted: October 06, 2020

1. INTRODUCTION

The magnetic properties of ferrites have been known to humanity since the discovery of the magnetite Fe_3O_4 as a natural ferrimagnetic material, which has been used in navigation compasses at the beginning of the 12^{th} century. Furthermore, since 1930, nanoferrites have been the subject of numerous investigations, which are essentially due to their interesting magnetic and electrical properties. However, the nanosized magnetic ferrites are characterized by the superparamagnetic behavior, the higher value of electrical resistivity, saturation magnetization and permeability *versus* low eddy current and dielectric losses with moderate dielectric constant [1, 2]. Consequently, these nanomaterials have been used in the manufacture of electrical transformer, antenna rods, memory chips, recording medium magnets, permanent magnets, transducers, activators [3 - 8], microwave [9], and as a result, they participate in meeting the recent nanotechnological demands. In fact, the interesting electrical and magnetic properties allow nanoferrites to cover almost all areas which are significantly related to their nanostructures, which are sensitively influenced by the preparation method, the agglomeration state, the proportion and the nature of metal oxides forming the matrix of the synthesized nanoferrite, the various additives included in the dopants and the impurities [10]. Moreover, in case of the spinel ferrites, with the general formula: AB_2O_4 (A = Co, Cu, Ni; B = Fe), there are two major structural variants: normal and inverse. However, in case of the

* Address correspondence to this author at the Laboratory of Resources, Materials and Ecosystem, Bizerta Science Faculty, Carthage University, 7021 Jarzouna, Bizerta, Tunisia; Tel: +216 72 590 613; Fax: +216 72 590566;
E-mail: BMWGEM@Gmail.com

normal spinel, the A cations occupy the tetrahedral interstitial sites, and the B cations occupy the octahedral interstitial sites. On the other hand, in case of the inverse spinel, B cations occupy all the tetrahedral and half of the octahedral sites, while the other A cations occupy the remaining half of the octahedral sites [10]. In particular, the cubic inverse spinel basic structure of cobalt ferrite has collinear ferromagnetic properties which are induced by the presence of permanent moment generated by antiparallel spins between Fe^{3+} and Co^{2+} cations, which are located at tetrahedral A-sites and octahedral B-sites, respectively. However, the substitution of cobalt by a suitable transition metal, M = Cr, Mn, Fe, Co, Ni, Cu, Zn, within the basic $CoFe_2O_4$ framework causes a remarkable improvement mainly in the chemical, structural, mechanical, electrical and magnetic properties, which allows to generate a wide range of novel interesting applications in diverse fields of the current modern technology [11]. On the other hand, it has been reported that the variation in Co, Cu and Zn in Co-Cu-Zn ferrite nanoparticles significantly enhances the electrical and magnetic properties and leads to a change in the lattice parameters [12]. Moreover, the substitution of Co^{2+} by Al^{3+} within the $CoFe_2O_4$ cubic inverse spinel basic structure causes a decrease in the particle size and saturation magnetization, whereas the chromium substituted cobalt ferrite nanoparticle series $Cr_XCoFe_{2-X}O_4(0 \leq X \leq 1)$ exhibits an excellent improvement in the structural and magnetic properties. Indeed, the variation of Cr^{3+} content leads to a change in saturation magnetization, particle size, band gap, lattice parameters and density [13]. Furthermore, in case of $Ni_XCo_{1-X}Fe_2O_4$(X = 0.2, 0.8) series, the lattice parameters decrease with the increase of Ni^{2+} composition and the change of preparation method from the sol-gel autocombustion to the coprecipitation leads to the decrease of lattice parameters and the increase of crystallite size and density [14].

In this present work, the most important purpose has been devoted to the study of the influence of copper substitution within the $CoFe_2O_4$ framework on the basic spinel structure, electrical and magnetic properties and therefore, for this reason, the copper substituted cobalt ferrite nanoparticle series with the nominal composition formula: $Cu_XCo_{1-X}Fe_2O_4$ (X = 0.0, 0.25, 0.5, 0.75, 1) has been synthesized *via* sol-gel self-combustion method [10]. The obtained black auto-combusted powders of the five synthesized ferrites have been analyzed by different physicochemical characterization techniques such as: X-Ray Powder Diffraction (XRPD), Fourier Transform Infrared spectroscopy (FTIR), Field Emission Scanning Electron Microscopy (FESEM) coupled to the Energy Dispersive X-ray spectroscopy (EDX), Complex Impedance Spectroscopy (CIS) and Superconducting Quantum Interference Device (SQUID) magnetic measurements.

2. METHODS

2.1. Chemical Synthesis

The series of five nanoferrites $Cu_XCo_{1-X}Fe_2O_4$ (X = 0, 0.25, 0.5, 0.75, 1) has been synthesized by the sol-gel self-combustion route [1] using suitable stoichiometric amounts of the following starting reactants: $Fe(NO_3)_3.9H_2O$(Sigma Aldrich, 98%), $Cu(NO_3)_2.6H_2O$(Sigma Aldrich, 98%), $Co(NO_3)_2.6H_2O$(Sigma Aldrich, 99%) and citric acid($C_6H_8O_7$, Sigma Aldrich, 99.5%), which have been dissolved in a minimum quantity of distilled water under magnetic stirring. Citric acid was taken in a 1:1 molar ratio to the metal cations and has also been used as a chelating agent and auto combustion fuel.

The obtained aqueous solutions of each explored composition X were heated at 80 °C under stirring, and at the same time, the pH was adjusted to 7 with an appropriate amount of concentrated ammonia solution leading to the formation of viscous black gels. The gels were slowly dried again by increasing the temperature to below 250 °C until reaching their corresponding autocombustion temperatures at which the dried gels ignited to form fractal loose precursor powders, which were slightly ground and then calcined at 900 °C for 2 hours leading to the formation of the five synthesized nanoferrites which are as follows:

S1M1(X = 0): ($CoFe_2O_4$);

S1M2(X = 0.25): ($Cu_{0.25}Co_{0.75}Fe_2O_4$);

S1M3(X = 0.5): ($Cu_{0.5}Co_{0.5}Fe_2O_4$);

S1M4(X = 0.75): ($Cu_{0.75}Co_{0.25}Fe_2O_4$);

S1M5(X = 1): ($CuFe_2O_4$).

2.2. Physiochemical Characterization Techniques

The structural characterizations by X-ray powder diffraction of the five calcined autocombusted powders at 900 °C during 2 h have been performed at 25 °C by using Philips X'Pert X-ray powder diffractometer (PANalytical, France), operating at the wavelength Cu-Kα radiation in the 2θ diffraction angle range 10-99 ° with the scan step of 0.02 ° and the counting time of 0.16 s. The Fourier transform infrared spectra for recording data were determined using NICOLET IR 200 FTIR spectrometer (Thermo Fisher Scientific, France), in the field of sweeping range 400-4000 cm^{-1}. The surface morphology and elemental composition analysis of the five studied nanoferrites have been analyzed by using MERLIN field emission scanning electron microscopy (Carl-Zeiss, France), coupled to the energy-dispersive X-ray spectroscopy, with a high resolution (0.8 nm and 1.4 nm at 15 kV and 1 kV, respectively). The electrical conductivity properties have been studied by complex impedance spectroscopy using the SI 1260 Impedance/Gain-Phase analyzer (Solartron Analytical, UK), with data acquisition frequency range of 10 Hz-32 MHz at intervals of 10 points per decade and under 100 mV applied voltage. The vacuum evaporation technique has been used for the gold electrode deposition on the two faces of each cylindrical pellet with a diameter of 13 mm, obtained by uniaxial compaction at a pressure of 120 MPa and sintered at 1173 K for 24 h. The electrical measurements have been carried out in the temperature range of 293-373 K with a 20 K increment. The magnetic measurement recording of both hysteresis loops, at 10 and 300 K, and ZFC-FC magnetization curves, in the temperature range of 10-300 K and under 500 Oe applied magnetic field, was performed by using MPMS SQUID magnetometer (Quantum Design, UK).

3. RESULTS AND DISCUSSION

3.1. X-ray Powder Diffraction Analysis

The five recorded X-ray powder diffractograms of the synthesized ferrites, Fig. (**1**), have similar profiles and clearly show only the single-phase corresponding to the five explored copper substituted cobalt ferrite nanoparticles: S1M1(X = 0.0); S1M2(X = 0.25); S1M3(X=0.5), S1M4(X=0.75) and S1M5(X=1). Indeed, the XRPD patterns have been indexed on the basis of the spinel face-centered cubic system with Fd3-m space group according to the JCPDS card file N° 00-022-1086 of $CoFe_2O_4$ and without any detection of additional phase peaks such as: CuO(JCPDS N° 99-200-4198, 99-200-3986); CoO(JCPDS N° 99-101-0211); FeO(JCPDS N° 99-200-3990, 99-200-3961, 99-200-2015); $CuFeO_2$(JCPDS N°99-200-2901, 99-100-0016) or Fe_2O_3(JCPDS N° 99-200-4059, 99-200-4032,99-200-2092, 99-200-0140). Consequently, the derived results from the XRPD acquisition data confirmed well that the five compositions are formed by a pure poly oriented nanocrystal with a single phase cubic spinel structure and suggested that the basic lattice stability of the five elaborated spinel ferrite nanoparticles did not chang during the substitution process of cobalt by copper within the parent cobalt ferrite basic structure when X composition increased from 0 to 1 [15]. Moreover, the lattice parameter determinations were performed by the least square fit refinement program, CELREFF [16], using the hkl and 2θ(°) values derived from the XRPD acquisition data.The crystallographic parameters of the unit cell of the five studied nanoferrites are listed in Table **1** .

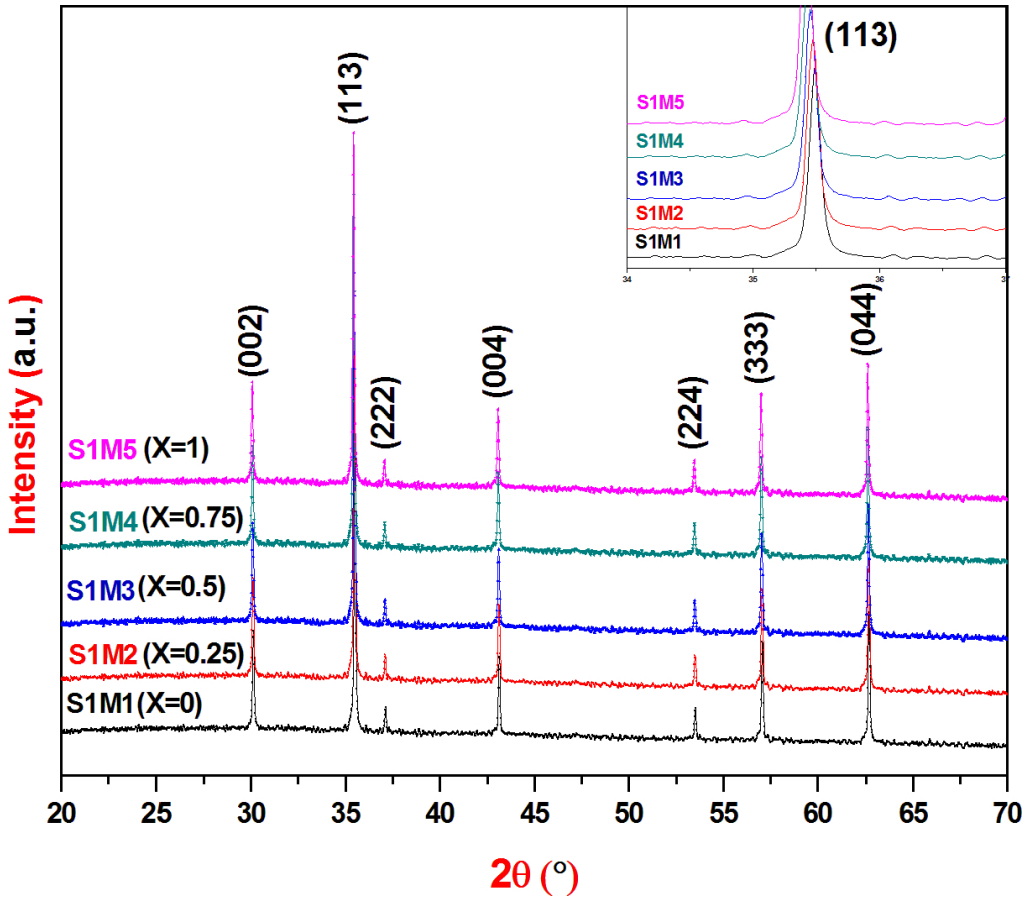

Fig. (1). XRP diffractograms of nanoferrites S1M1-5.

Table 1. Refined lattice parameters and crystallite size calculations of nanoferrites S1M1-5

Nanoferrite	a(Å)	Space Group	D_{XRPD}(nm)
S1M1(X = 0)	8.389(3)	Fd3-m	19.96
S1M2(X = 0.25)	8.393(1)	Fd3-m	20.93
S1M3(X = 0.5)	8.397(6)	Fd3-m	21.84
S1M4(X = 0.75)	8.401(2)	Fd3-m	23.01
S1M5(X = 1)	8.405(5)	Fd3-m	24.94

In addition, during the substitution procedure, the increase of Cu content from 0 to 1 caused a slight displacement of XRPD peaks toward lower 2θ diffraction angles compared to those of the parent ferrite $CoFe_2O_4$. In particular, as clearly shown in the upper right inset of Fig. (**1**), the observed 2θ low shift, from 2θ[$CoFe_2O_4$(X=0)] = 35.49 ° to 2θ[$CuFe_2O_4$(X=1)] = 35.42 °, in case of the Bragg reflection (1 1 3), is due to the slight increase in the unit cell parameter, from a[$CoFe_2O_4$] = 8.389(3) Å to a[$CuFe_2O_4$] = 8.405(5) Å, Table **1** , which is induced by the low difference between cationic radius values of cobalt and copper: r(Co^{2+}) = 0.72 Å; r(Cu^{2+}) = 0.73 Å.

Moreover, the crystallite size value D was calculated using Scherrer equation [17]:

$$D = \frac{0.9\lambda}{\Delta(2\theta)\cos\theta}$$

Where λ is the wavelength of the CuKα (1.54187 Å), Δ(2θ) is the full width at the half maximum (FWHM) of the (1 1 3) diffraction peak in radian, and θ is the Bragg's angle.

The crystallite size calculation values illustrated in Table **1** , prove well the nanocrystallinity of the five explored ferrites and seem to be increased with X composition from D_{XRPD}[$CoFe_2O_4$] = 19.96 nm to D_{XRPD}[$CuFe_2O_4$]= 24.94 nm.

On the other hand, in case of $Cu_XCo_{1-X}Fe_2O_4$ (X = 0, 0.3, 0.5, 0.7, 1) series, a similar work synthesized by the coprecipitation technique [13], the investigators mentioned that during the substitution process, when X copper content increased from 0 to 1, both the calculated unit cell parameter and the estimated crystallite size *via* Scherrer equation decreased mutually as follows: from a[$CoFe_2O_4$(X =0)] = 8.354(2) Å to a[$CuFe_2O_4$(X =1)] = 8.311(2) Å and from D[$CoFe_2O_4$] = 30 nm to D[$CuFe_2O_4$] = 18 nm, respectively. This declared that the slow linear decreasing trend in the unit cell parameters is attributed to the replacement of the larger ionic radius of Co^{2+} by the smaller ionic radius of Cu^{2+} in the host system. Moreover, the latest rendition seems to be in contradiction with the ionic radius values of Co^{2+}(0.70 Å) and Cu^{2+}(0.73Å), cited previously in the same work [13], because logically, the refined lattice parameter value should increase with X Cu^{2+} content increase, which has the larger cationic radius compared to that of Co^{2+} cation and consequently, such interpretation is in coherence with the XRPD results reported herein.

3.2. Fourier Transform Infrared Spectroscopy

In order to further investigate the crystal structure, vibrational FTIR spectroscopy measurements have been performed. However, the FTIR spectra of the five studied nanoferrites, Fig. (**2**), show the presence of two main absorption bands centered at the following frequency values: 410 cm^{-1} and 595 cm^{-1}, characteristic of the typical vibrational modes of monophasic cubic spinel structure and thus can be attributed to the intrinsic vibration modes of octahedral (16d special position) and tetrahedral (8a special position) sites, respectively within the ferrite crystal network [18, 19]. Moreover, the average values of these previous two absorption bands are coherent with those reported in a similar work using the coprecipitation method as the synthesis technique [13 - 19]. In addition, it can be deduced that the FTIR study results are in good agreement with those of XRPD, which confirm well that the five synthesized nanoferrites are pure single phases with cubic spinel crystal network.

3.3. FESEM-EDX Analysis

The FESEM micrographs Fig. (**3**) have allowed to conclude that the observed morphologies of the five explored nanoferrites are roughly similar and are composed of a uniform grain size distribution with angular shapes, correlating the one observed in the $CoFe_2O_4$ FESEM micrograph [20]. The average grain sizes vary between D_{FESEM}(S1M1) = 22.05 nm and D_{FESEM}(S1M5) = 27.17 nm, whose values seem to be relatively higher than those calculated by Scherrer equation, D_{XRPD}, and Langevin function fitting, D_{LFF}, using XRPD and SQUID magnetic data, respectively. However, the presence of dead magnetic layers on the particle surfaces within the five studied nanostructures could explain the origin of the observed grain size difference between D_{FESEM} and D_{LFF} [21]. Moreover, as shown in the lower-left inset of Fig. (**3**) (S1M1 and S1M5), the EDX spectra of elementary qualitative analysis indicate the presence of constituent elements of $CoFe_2O_4$ and $CuFe_2O_4$, respectively. The analysis results of elemental compositions of the five Cu-substituted cobalt ferrite nanoparticles listed in Table **2** are in good agreement with the nominal formula of each nanoferrite.

In addition, the information derived from the XRPD, FTIR and FESEM-EDX data allow concluding that the used sol-gel autocombusted process is the promising synthesis technique which leads to the elaboration of pure fine powders and the cubic spinel basic host lattice has been integrally preserved during the substitution procedure which is due to the slight cationic radius difference between Cu^{2+} and Co^{2+}.

Table 2. EDX elemental composition of nanoferrites S1M1-5.

Nanoferrite	Atomic Percentage (%)			
	Co	**Cu**	**Fe**	**O**
S1M1	14.53(0.20)	–	28.56(0.28)	56.91(0.24)
S1M2	11.04(0.22)	3.74(0.14)	28.40(0.18)	56.82(0.26)
S1M3	7.37(0.17)	7.52(0.25)	28.37(0.23)	56.74(0.21)
S1M4	10.95(0.22)	3.84(0.27)	28.42(0.16)	56.79(0.29)
S1M5	–	14.48(0.19)	28.67(0.23)	56.85(0.25)

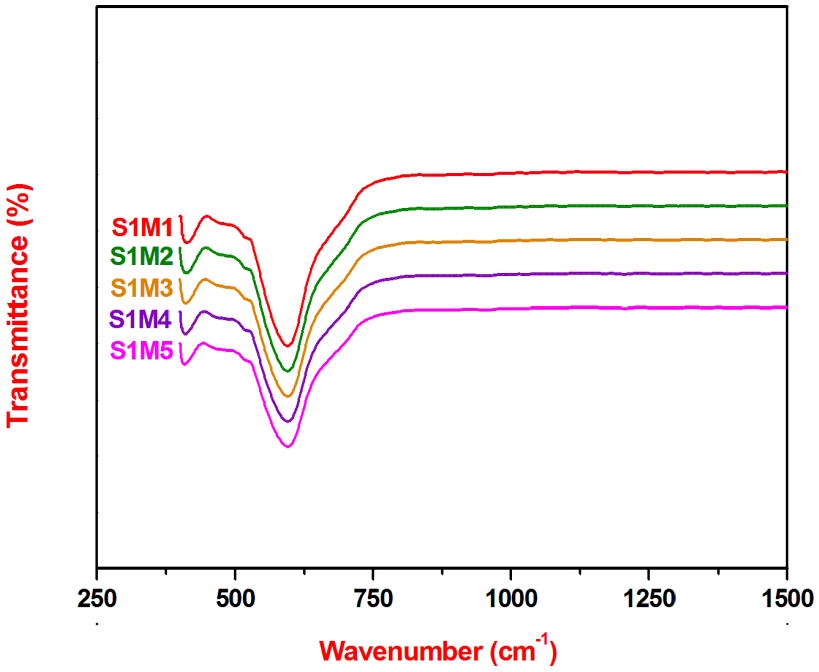

Fig. (2). FTIR spectra of nanoferrites S1M1-5.

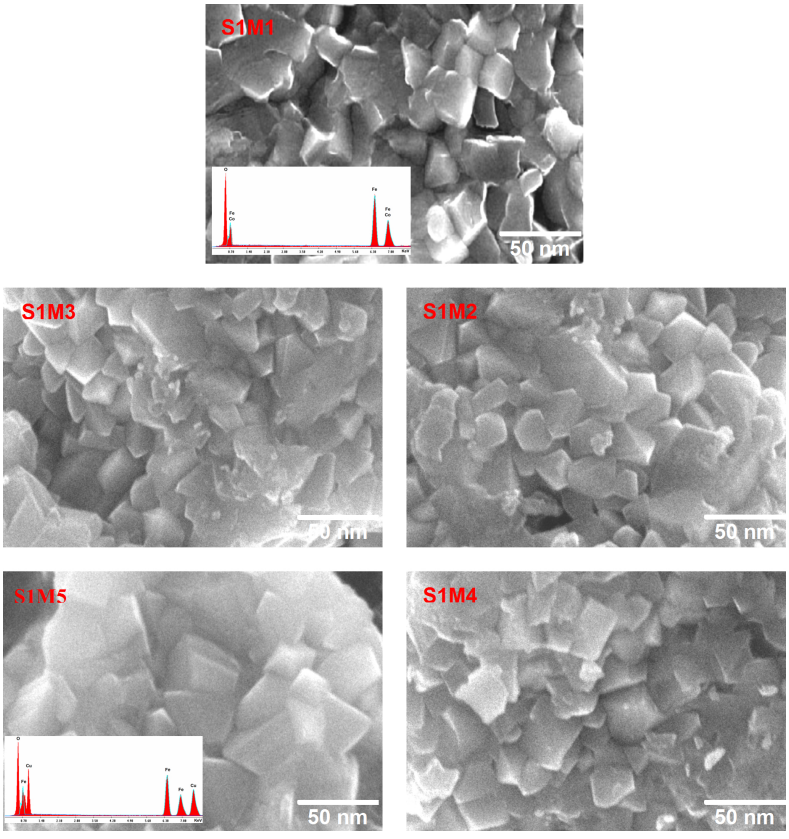

Fig. (3). FESEM micrographs of nanoferrites S1M1-5.

3.4. Complex Impedance Spectroscopy

The Nyquist diagrams of the five explored copper substituted cobalt ferrites, in the temperature range 293-373 K, have similar profiles. As shown in Fig. (**4a**) the presence of a single semicircular arc in the recorded impedance diagram of $CoFe_2O_4$[X=0] is an indication that the electrical conduction behavior is mainly due to the corresponding bulk resistance with the absence of the grain boundary effect [20 - 22]. However, in this case, the direct current conductivity value has been calculated by the following equation: $\sigma_{DC}=\frac{E}{R_{DC}.S}$, where E and S are the thickness and the surface of the used pellet

respectively, R_{DC} is the bulk resistance value determined at the five selected experimental temperatures from the semicircle intercept on the real axis in the corresponding Nyquist diagram plots. In addition, the representative curves of $\ln(\sigma_{DC})$ *versus* $\frac{10^3}{T}$ of the selected nanoferrites, Fig. (**4b**), show a linear trend and well fit the Arrhenius equation $\sigma_{Tot} = \sigma\exp(-E_a/K_BT)$, where σ is the preexponential factor, E_a is the activation energy of electrical conduction, K_B is the Boltzmann constant and T is the absolute temperature. Moreover, the increased electrical conductivity observed with temperature increase shows that the conducting behavior is an activated thermally process and as a result, allows to calculate the activation energy value from the corresponding plot slope obtained from fitting data of each studied nanoferrite. Based on the electrical property results derived from Table **3** , which are in good agreement with those reported in the bibliographic data [23 - 27], the DC electric conductivity of the five explored nanoferrites is found to increase with increasing temperature from 293 K to 373 K and at fixed X composition. Indeed, in case of $CoFe_2O_4$[X=0], the DC conductivity value increases up to twenty orders of magnitude, whereas in case of $CuFe_2O_4$[X=1], the conductivity increase reaches ten orders only. The best DC electrical conductivity value $\sigma_{DC}(373K) = 27.03x10^{-3}S.cm^{-1}$ has been observed at 373 K for $CuFe_2O_4$[X = 1] nanoferrite with an associated lower activation energy of 0.269 eV. The observed phenomenon could be attributed to the increased electrical charge carrier drift mobility and also indicates the presence of semiconductor like behavior. On the other hand, at a fixed temperature, the DC electrical conductivity raises six and three orders of magnitude at 293 K and 373 K, respectively. In addition, the mentioned previous electrical conductivity growth with X composition increase from 0 to 1 could be originated from the difference between the elementary electrical conductivity of both transition metals Co(0.172 $S.cm^{-1}$) and Cu(0.294 $S.cm^{-1}$), showing an improvement in the conductivity value by an increase of charge carrier concentration when copper content increases from 0 to 1, and consequently, leading to the activation energy value decrease from E_a(S1M1) = 0.345 eV to E_a(S1M5) = 0.269 eV. Furthermore, in order to identify the electrical conduction mechanism within the five explored nanoferrite frameworks, the study of alternating current conductivity σ_{AC} variation has been carried out in the experimental frequency range. However, in case of S1M5 nanoferrite, the graphical representation of $\ln(\sigma_{AC})$ as a function of ln(f), Fig. (**5a**), shows the linear portion in the curve in the lower frequency range, followed directly by a plot exponential increase with frequency in the higher frequency domain which suggests that the mentioned AC electrical conduction mechanism in the host system follows the Jonsher's universal power law equation:$\sigma_{AC} = \sigma_{DC} + P\omega^n$

Wherein n, ω and P are the dimensionless angular frequency exponent, angular frequency and temperature-dependent constant, respectively [28]. In addition, the numeric values of n = 2, P(373 K) = $4.405x10^{-16}$ $S.cm^{-1}.rad^{-1}$ and σ_{DC}(373 K) = 0.0277 $S.cm^{-1}$, have been determined by using the second order polynomial fitted curve of σ_{AC}(373 K) *versus* frequency of S1M5 nanoferrite, Fig. (**5b**), which has the highest electrical conductivity value at 373 K, with an R-square value equal to 0.9999. Furthermore, the previous fitted value of σ_{DC} (373 K) = 0.0277 $S.cm^{-1}$ is very close to that derived from S1M5 impedance diagram recorded at 373 K, whose value is equal to 0.0270 $S.cm^{-1}$. Consequently, the charge carrier transport occurs according to the electron hopping exchange between ferrous Fe^{2+} and ferric Fe^{3+} cations which are located at randomly equivalent crystallographic sites in the applied electrical field direction [29 - 31].

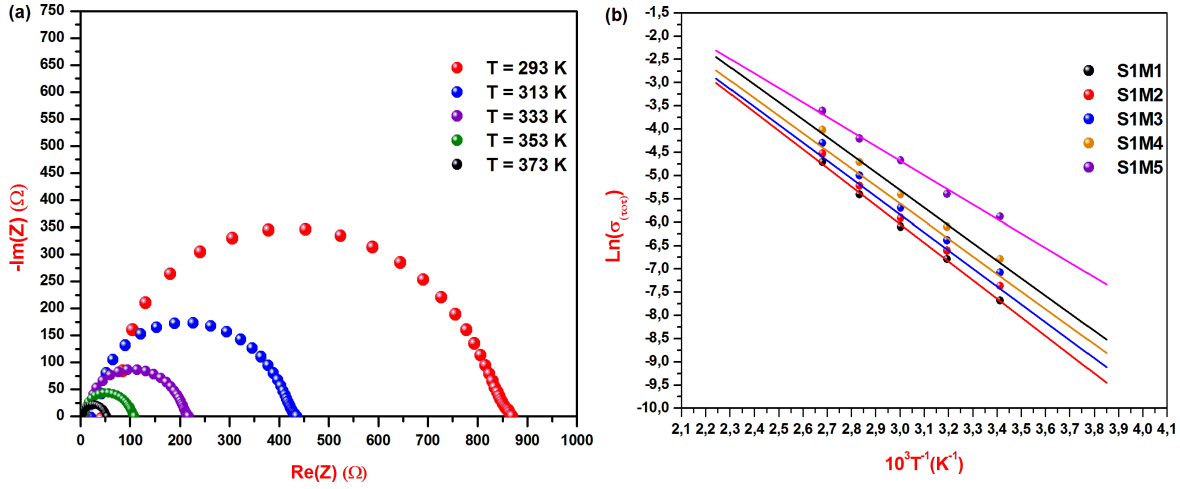

Fig. (4). (**a**) Impedance diagram of the nanoferrite S1M1 in the temperature range 293-373 K. (**b**) Arrhenius plot of nanoferrites S1M1-5.

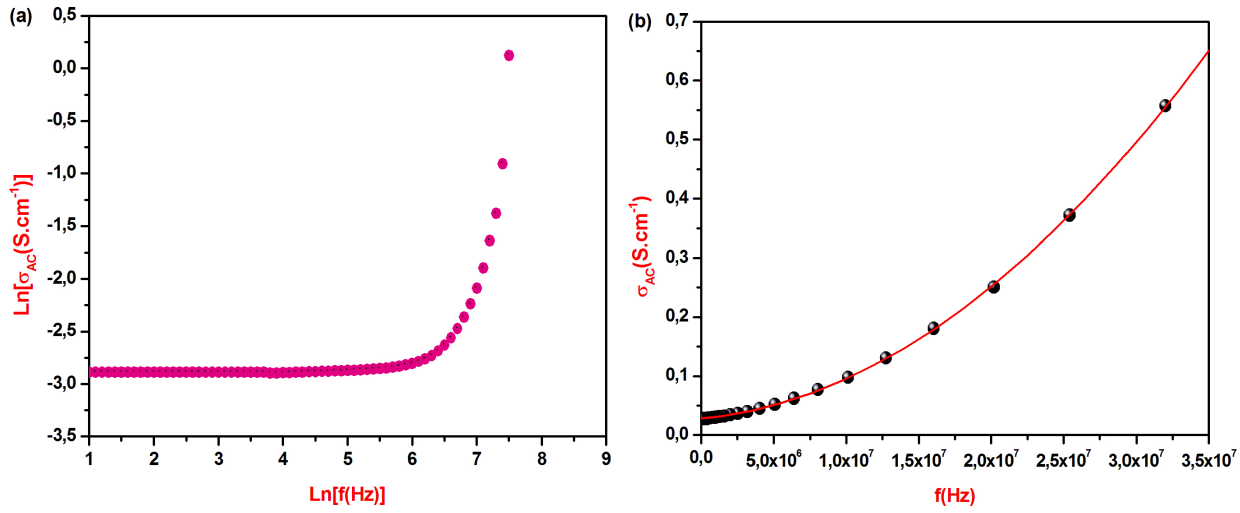

Fig. (5). (**a**) Graphic representation of Ln(σAC) *versus* Ln(f) of nanoferrite S1M5.
(**b**) Second order polynomial fitted curve of σAC(373 K) versus frequency of nanoferrite S1M5.

3.5. SQUID Magnetometry

As shown in Fig. (**6a**), the recorded ZFC-FC magnetization curves in the temperature range 10-300 K and under 500 Oe applied magnetic field have allowed determining the blocking temperature of each studied nanoferrite, T_B, which is situated at the first intersection special point between ZFC and FC curves. However, the deduced blocking temperature values from their corresponding ZFC-FC curves: T_B(S1M1) = 285.15 K, T_B(S1M2) = 280.93 K, T_B(S1M3) = 277.24 K, T_B(S1M4) = 273.81 K, T_B(S1M5) = 270.57 K, seem to be decrease with the increase of X copper composition. Indeed, in case of $CoFe_2O_4$[X=0] cubic spinel basic structure, Fe^{3+} metallic cations with $3d^5$ electronic configurations create high spin states and their orbital angular moments are trapped in a weak ligand field. As a result, the magnetic magnitude anisotropy contribution should be mainly determined from the strong L-S coupling strength of Co^{2+} metallic cations with $3d^7$ electronic configurations at the octahedral sites, which generate a large magnetocrystalline anisotropy constant and consequently lead to the high magnetocrystalline anisotropy energy barrier value. Moreover, the observed decrease of anisotropy constant value from K[S1M1(X=0)] = 5.08 erg.cm^{-3} to K[S1M5(X=1)] = 1.63 erg.cm^{-3}, with X copper incorporation increase from 0 to1, is mainly due to the lower Cu^{2+} L-S coupling contribution compared to that of Co^{2+} and thus, that leads to the previously mentioned decrease in the blocking temperature value, which also seems to decrease with the increase in particle size. However, such interpreted results are in coherence with the equation $T_B = \frac{KV}{25K_B}$, which is derived from the magnetocrystalline anisotropy constant K reported hereafter.

Moreover, the presence of bifurcation between ZFC and FC curves proves well that the five explored nanoferrites which are initially ferrimagnetic at the blocked regime transit to the superparamagnetic regime above the blocking temperature T_B which is characterized by the dominance of magnetic single domains. Within these domains, the magnetic anisotropy energy barrier value, KV, becomes smaller than the thermal energy value, K_BT, leading to the deblocking of magnetic moment switchability to the applied field which caused the transition to the superparamagnetic state, obeying to the Curie-Weiss law [32, 33]. In addition, the five ZFC profiles exhibit a linear region starting from 10 K which corresponds to the tendency to saturation accompanied directly by a large increase in the magnetization magnitude up to the blocking temperature, while a trend to the saturation has been observed in the five ZF magnetization curves, which confirms the presence of strong A-B dominant dipolar interactions [34]. The previously mentioned typical superparamagnetic behavior has been observed in a similar work devoted to the cobalt ferrite nanoparticles [34].

As can be seen from the 10 K magnetic hysteresis loops in Fig. (**6b**) the five studied copper-substituted cobalt ferrite nanoparticles are in blocked regime which obeys to the Stoner-Wolhfarth law [35]. However, the absence of hysteresis in the 300 K M-H curves, as shown in Fig. (**7a**), is an indication of superparamagnetic behavior and as a result, the five explored nanoferrites can be considered as magnetic single domains. In addition, the observed increase in saturation magnetization values M_S at 10 K compared to those at 300 K could be originated from the magnetic moments under the applied field direction which is strongly influenced by the mutual competition state between the magnetocrystalline anisotropy energy and the thermal energy as a function of temperature. In fact, the random orientation of magnetic moments becomes dominant above the blocking temperature at which the thermal energy value overcomes that of anisotropy energy. Moreover, the 300 K saturation magnetization value 55.97 emu/g, Table **4**, is very close to that cited in the case of $CoFe_2O_4$ nanocrystals, 56.7 emu/g, but is less than that of the bulk counterpart value 80 emu/g [35]. In fact, the presence of surface spin canting orientation, forming a core and shell within the magnetic ferrite nanoparticle structure, is essentially due to the surface spin disordering and magnetic dead layers at the surfaces, which are generally considered to be responsible for the reduced saturation magnetization magnitude of the five studied nanoferrite crystal lattices with respect to their bulk parent basic structure.

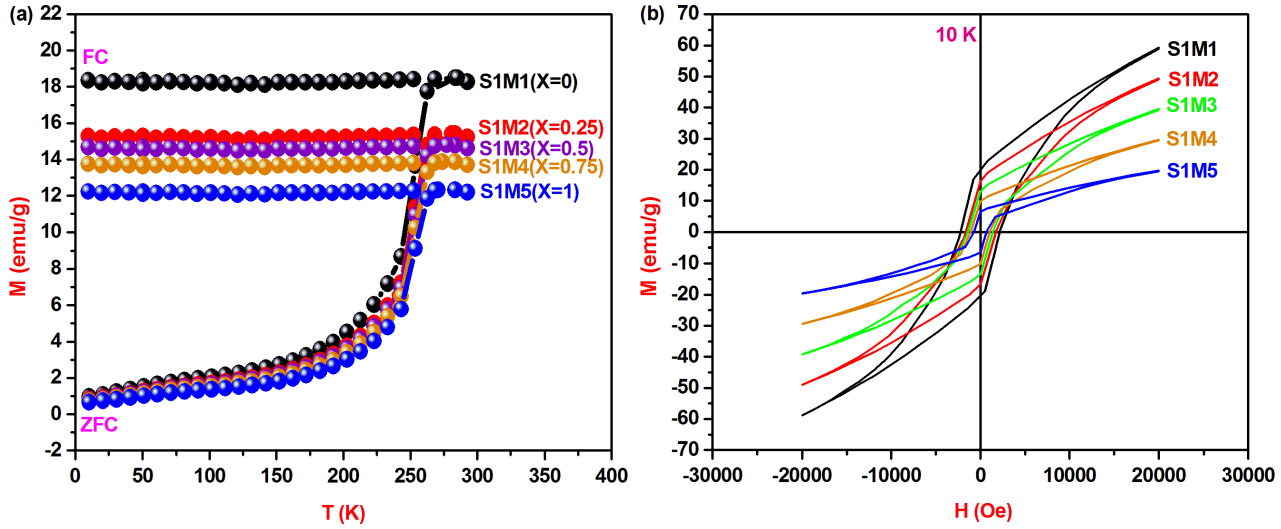

Fig. (6). (**a**) The ZFC-FC magnetization curves of the nanoferrites S1M1-5 recorded in the temperature range 10-300 K and under 500 Oe magnetic field. (**b**) The 10 K hysteresis loops of the nanoferrites S1M1-5.

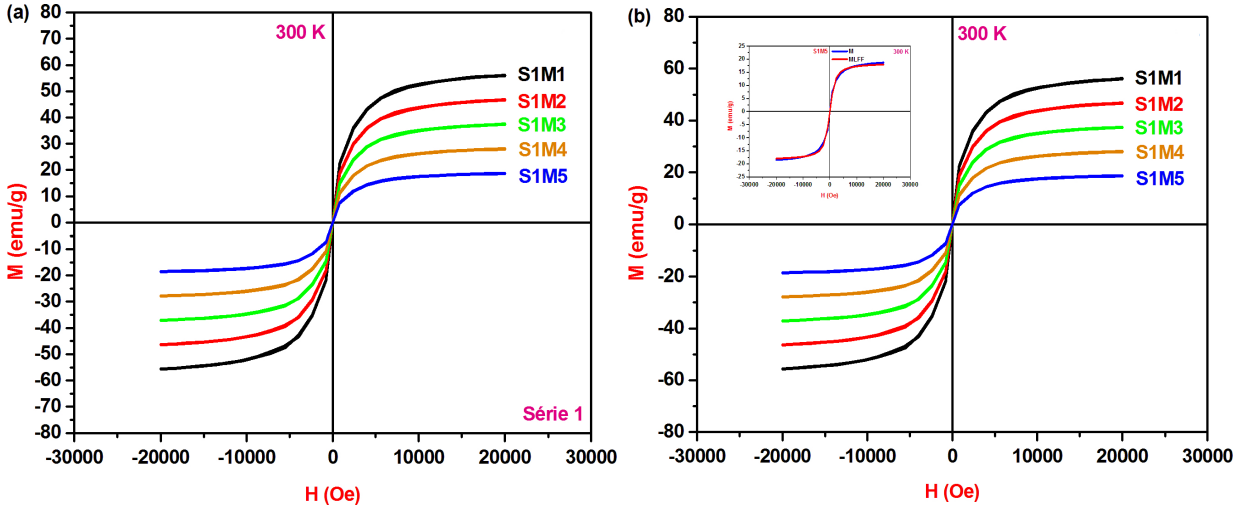

Fig. (7). (**a**) The 300 K hysteresis loops of the nanoferrites S1M1-5.
(**b**) Langevin function fitted superparamagnetic M-H curves of the nanoferrites S1M1-5.

Table 3. Electric properties of nanoferrites S1M1-5.

Nanoferrite	$\sigma_{DC(293K)}$ (S.cm^{-1})	$\sigma_{DC(313K)}$ (S.cm^{-1})	$\sigma_{DC(333K)}$ (S.cm^{-1})	$\sigma_{DC(353K)}$ (S.cm^{-1})	$\sigma_{DC(373K)}$ (S.cm^{-1})	E_a(eV)
S1M1	$4.606x10^{-4}$	0.00113	0.00225	0.00450	0.00900	0.345
S1M2	$6.322x10^{-4}$	0.00135	0.00270	0.00540	0.01081	0.332
S1M3	$8.444x10^{-4}$	0.00169	0.00338	0.00676	0.01351	0.325
S1M4	0.00113	0.00225	0.00450	0.00901	0.01801	0.323
S1M5	0.00279	0.00453	0.00934	0.01493	0.02703	0.269

Table 4. Magnetic properties measured at 10 K and 300 K of nanoferrites S1M1-5

Nanoferrite	10 K			300 K		
	H_c(Oe)	M_r(emu/g)	M_s(emu/g)	H_c(Oe)	M_r(emu/g)	M_s(emu/g)
S1M1	2179	20.00	59.22	0	0	55.97
S1M2	1729	16.33	49.35	0	0	46.64
S1M3	1386	12.96	39.48	0	0	37.31
S1M4	1036	10.00	29.59	0	0	27.97
S1M5	693	6.52	19.73	0	0	18.64

On the other hand, in case of the cubic spiel ferrite structure AB_2O_4, Neel [36] has reported that the magnetic properties seem to be strongly sensitive to the metallic cation nature and the distribution method into the A(8a) tetrahedral and B(16d) octahedral crystallographic sites which result in predominant A-B dipolar interactions between A and B metallic cations which are generated by the orientation in opposite directions of the magnetic moments of A and B sublattice whose resultant magnitude value determines the net magnetic moment intensity value of the lattice which is equal to $M_L = \sum M_B - \sum M_A$. However, both M-H curves of the five explored nanoferrites, recorded on SQUID at 10 and 300 K, show the decrease of saturation magnetization with the increased Cu^{2+} content from 0 to 1, which is mainly influenced by the electron magnetic dipole moment magnitude that depends on the metallic cation nature inside the two A and B sublattice sites. Indeed, within the cubic inverse spinel ferrite basic framework $CoFe_2O_4$[X = 0], the Fe^{3+}(5 μ_B) cations are distributed evenly between A and B sublattice sites, while the Co^{2+}(3 μ_B) cations occupy only B sublattice sites. Furthermore, the latest substitution derivative $CuFe_2O_4$[X = 1], has been identified as a cubic inverse spinel structure within which the Cu^{2+}(1 μ_B) cations have a strong specific affinity to occupy the B octahedral sublattice sites imposed by the crystal field stabilization energy of metallic cation occupation in spinel sublattice sites [37]. However, the net magnetic moment calculation values M_L of the five studied nanoferrites: S1M1(3μ_B per molecule); S1M2(2.5μ_B per molecule); S1M3(2μ_B per molecule); S1M4(1.5μ_B per molecule) and S1M5(1μ_B per molecule), seem to be decreased with the increase of Cu^{2+} content from 0 to 1, which leads to the observed magnitude reduction of saturation magnetization M_S.

According to the magnetic theory, the magnetic behavior can be subdivided on the basis of particle size into four domains: superparamagnetic domain (SPMD), single domain (SD), pseudo-single domain (PSD) and the multidomain (MD). The specific transition from the MD state to the SD one occurs when the particle reaches the magnetic single domain critical size D_c(LFF), which strongly depends on magnetocrystalline energy magnitude. Likewise, the transition from the MD state to the SPMD one is reached below the supercritical threshold size called the superparamagnetic particle diameter D(LFF). Thus, in case of SPMD state, particles are in SD and consequently, both remanence and coercivity values are close to zero. However, the magnetization magnitude M *versus* both magnetic field H and absolute T obeys to the following mathematic equation: $M = M_s.L(x)$

Where L(x) is the Langevin function, $x = x = \frac{\mu_P.H}{K_B.T}$, M_s is the saturation magnetization, μ_p is the particle magnetic moment, μ_B is the Bhor magneton, N_P is the number of particles per unit mass contributing to the magnetization and K_B is the Boltzmann constant.

The magnetic anisotropy constant value K can be determined by the following expression:

$$K = \frac{25K_BT_B}{V}$$

Where T_B and V are the blocking temperature of the sample and the volume of the single particle, respectively.

In case of MD-SD spherical nanoparticle transition, the critical diameter value D_c of the magnetic single domain can be calculated by the following relation [38]:

$$D_c = \frac{18\sqrt{AK}}{\mu_0 M_s^2}$$

Wherein A is the stiffness constant.

In order to further investigate magnetic features, Langevin function fitting on the 300 K superparamagnetic M-H data of the five explored nanoferrites, Fig. (**7b**), has been used to calculate the following superparamagnetic parameters: M_s(LFF), μ_p, D(LFF), K, N_P and D_c(LFF) which are summarised in Table **5**.

Table 5. Fit parameters values of M_s(LFF), D(LFF), D_C(LFF), μ_p, K and N_P, with the corresponding R^2 fit goodness factors of nanoferrites S1M1-5.

Nanoferrite	M_s (emu/g)	$M_{s(LFF)}$ (emu/g)	D_{XRPD} (nm)	D_{LFF} (nm)	$D_{C(LFF)}$ (□m)	μ_p (μ_B)	N_P (10^{17}/g)	Kx10^5 (erg/cm^3)	R^2
S1M1	55.97	53.86	19.96	17.18	3.174	5943	9.77	5.08	0.9994
S1M2	46.64	44.89	20.93	17.62	4.206	5940	8.14	4.19	0.9994
S1M3	37.31	35.91	21.84	18.19	5.930	5938	6.52	3.32	0.9994

(Table 5) contd.....

Nanoferrite	M_s (emu/g)	$M_{s(LFF)}$ (emu/g)	D_{XRPD} (nm)	D_{LFF} (nm)	$D_{C(LFF)}$ (□m)	μ_p (μ_B)	N_P (10^{17}/g)	$Kx10^5$ (erg/cm^3)	R^2
S1M4	27.97	26.92	23.01	19.01	9.212	5934	4.89	2.47	0.9994
S1M5	18.64	17.95	24.94	20.30	17.092	5932	3.26	1.63	0.9994

In addition, it can be deduced from the theoretical calculation results illustrated in Table **5** that the calculated values of M_s(LFF) and D(LFF) by Langevin function fitting, (LFF), are in good agreement with those determined from the experimental data: M_s(300 K) and D(XRPD), and the large values of magnetocrystalline anisotropy constants are basically due to the presence of strong L-S couplings between Cu^{2+}(1 μ_B), Co^{2+}(3 μ_B) and Fe^{3+}(5 μ_B) cations which are distributed over the tetrahedral and octahedral of the inverse spinel structure, whose value seems to decrease with the increase of X Cu^{2+} composition from K[S1M1(X = 0)] = 5.08x10^5 erg.cm^{-3} to K[S1M5(X = 1)] = 1.63x10^5 erg.cm^{-3}. Moreover, the increase of D_C(LFF) value with the decrease of M_S could be due to the magnetic moment difference between Cu^{2+}(1 μ_B) and Co^{2+}(3 μ_B) cations. Indeed, during the substitution procedure when Cu^{2+} composition increases from 0 to 1, at the same time Co^{2+}(3 μ_B), composition decreases from 1 to 0 and hence, the induced decrease in M_S magnitude leads to the increase in D_C(LFF) value which enhances the SD state size within the basic framework. Moreover, the calculated D_C(LFF) values of the five studied nanoferrites: D_C[S1M1(X = 0)] = 3.174 μm; D_C[S1M2(X = 0.25)] = 4.206 μm; D_C[S1M3(X = 0.5)] = 5.930 μm and D_C[S1M4(X = 0.75)] = 9.122 μm], are lower than that of the hematite SD-MD transition particle size D_C = 15 μm, whose value is slightly lower than that of S1M5: D_C[S1M5(X = 1)] = 17.092 μm.

CONCLUSION

Through the present investigation, nanocrystalline ferrite series $Cu_XCo_{1-X}Fe_2O_4$ (X = 0, 0.25, 0.5, 0.75, 1), has been elaborated *via* sol-gel autocombustion classic process. The information derived from the XRPD, FTIR and FESEM-EDX study results allowed us to conclude that the five synthesized ferrites were identified as cubic spinel single phase and their corresponding pure fine powders were composed of homogeneous nanoparticles with size range 19.96-24.94 nm. In fact, during the substitution procedure, when X copper composition increased from 0 to 1, the cubic spinel basic structure was preserved for the five studied nanoferrites. On the other hand, an increase was observed in the lattice parameter, crystalline size and electrical conductivity values *versus* a decrease in the blocking temperature, magnetocrystalline anisotropy constant, saturation magnetization, remanance and coercivity values. Furthermore, the room temperature superparamagnetic behavior has been confirmed *via* the SQUID magnetometry measurements. In addition, Langevin function fitting on M-H(300 K) data has been used to perform the theoretical calculations of superparamagnetic parameters which seem to be mainly influenced by both X copper content and particle size effect.

Interestingly, the main features of the five explored nanoferrites highlighted by the physicochemical characterizations include: good homogeneous nanocrystallinity, remarkable electrical conductivity properties, excellent magnetic properties as ferrimagnetic nanoferrites with high magnetocrystalline anisotropy energy, moderate saturation magnetization, high coercivity, strong (L-S) coupling and small room temperature superparamagnetic size act as the most suitable promising candidates for various special potential nanotechnological applications such as: magnetic resonance imaging, manufacture of electrical motor and electrochemical gas sensors, photocatalysis, drug delivery particularly in chemotherapeutic treatments, magnetic separation, information storage devices and antibacterial activity against Escherichia Coli bacteria[E. Coli].

CONSENT FOR PUBLICATION

Not applicable.

AVAILABILITY OF DATA AND MATERIALS

Not applicable.

FUNDING

The present work has been supported by the Ministry of Higher Education and Scientific Research of Tunisia.

CONFLICT OF INTEREST

The authors declare no conflict of interest, financial or otherwise.

ACKNOWLEDGEMENTS

The Authors acknowledge the support by the Ministry of Higher Education and Scientific Research of Tunisia.

REFERENCES

[1] Mishra, S.; Karak, N.; Kundu, T.K.; Das, D.; Maity, N.; Chkravorty, D. Nanocrystalline nickel ferrites prepared by doping with niobium ions. *Mater. Lett.,* **2006**, *60*, 1111-1115. [http://dx.doi.org/10.1016/j.matlet.2005.10.085]

[2] Maaz, K.; Karim, S.; Mumtaz, A.; Hasanain, S.K.; Liu, J.; Duan, J.L. Synthesis and magnetic characterization of nickel ferrite nanoparticles prepared by co-precipitation route. *J. Magn. Magn. Mater.,* **2009**, *321*, 1838-1842. [http://dx.doi.org/10.1016/j.jmmm.2008.11.098]

[3] Murdock, E.S.; Simmons, R.F.; Davidson, R. Roadmap for 10 Gbit/in/sup 2/ media: Challenges. *RIEEE Trans. Magn.,* **1992**, *28*, 3078-3083. [http://dx.doi.org/10.1109/20.179719]

[4] Kim, W.; Lee, S.; Kim, C. Growth of ultrafine NiZnCu ferrite and magnetic properties by a sol–gel method. *J. Magn. Magn. Mater.,* **2001**, *1418*, 226-230. [http://dx.doi.org/10.1016/S0304-8853(01)00029-4]

[5] Satyanarayana, L.; Reddy, K.M.; Manorama, S.V. Nanosized spinel $NiFe_2O_4$: A novel material for the detection of liquefied petroleum gas in air. *Mater. Chem. Phys.,* **2003**, *82*, 21-25. [http://dx.doi.org/10.1016/S0254-0584(03)00170-6]

[6] Wang, X.; Li, L.; Su, S.; Yue, Z. Electromagnetic properties of low-temperature-sintered $Ba_3Co_{2-x}Zn_xFe_{24}O_{41}$ ferrites prepared by solid state reaction method. *Magn. Magn. Mat.,* **2004**, *280*(1), 10-13. [http://dx.doi.org/10.1016/j.jmmm.2004.02.016]

[7] Rana, S.; Gallo, A.; Srivastava, R.S.; Misra, R.D.K. On the suitability of nanocrystalline ferrites as a magnetic carrier for drug delivery:

Functionalization, conjugation and drug release kinetics. *Acta Biomater.,* **2007**, *3*(2), 233-242.
[http://dx.doi.org/10.1016/j.actbio.2006.10.006] [PMID: 17224313]

[8] Kharabe, R.G.; Devan, R.S.; Kanamadi, C.M.; Chougule, B.K. Structural and electrical properties of Cd-substituted Li–Ni ferrites. *J. Alloys Compd.,* **2008**, *463*, 67-72.
[http://dx.doi.org/10.1016/j.jallcom.2007.09.061]

[9] Zhao, H.; Sun, X.; Mao, Ch.; Du, J. Preparation and microwave–absorbing properties of $NiFe_2O_4$-polystyrene composites. *Physica B,* **2009**, *404*(1), 69-72.
[http://dx.doi.org/10.1016/j.physb.2008.10.006]

[10] Sutka, A.; Mezinskis, G. Frontiers of Materials Science, Sol-gel auto-combustion synthesis of spinel-type ferrite nanomaterials. *Mater. Sci.,* **2012**, *6*(2), 128-141.

[11] Pubbya, K.; Babub, K.V.; Narang, S.B. Magnetic, elastic, dielectric, microwave absorption and opticalcharacterization of cobalt-substituted nickel spinel ferrites. *Mater. Sci. Eng. B,* **2020**, *255*114513
[http://dx.doi.org/10.1016/j.mseb.2020.114513]

[12] Jasrotia, R.; Puri, P.; Verma, A.; Singh, V.P. Magnetic and electrical traits of sol-gel synthesized Ni-Cu-Zn nanosizedspinel ferrites for multi-layer chip inductors application. *J. Solid State Chem.,* **2020**, *289*121462
[http://dx.doi.org/10.1016/j.jssc.2020.121462]

[13] Samavati, A.; Ismail, A.F. Antibacterial properties of copper-substituted cobalt ferrite nanoparticles synthesized by co-precipitation method. *Particuology,* **2017**, *30*, 158-163.
[http://dx.doi.org/10.1016/j.partic.2016.06.003]

[14] Bharambea, S.S.; Trimukheb, A.; Bhatia, P. Synthesis techniques of nickel substituted cobalt ferrites – aninvestigative study using structural data. *Mater. Today: Proceedings,* **2020**, *23*, 373-381.

[15] Raju, K.; Venkataiah, G.; Yoon, D.H. Effect of Zn substitution on the structural and magnetic properties of Ni–Co ferrites. *Ceram. Int.,* **2014**, *40*, 9337-9344.
[http://dx.doi.org/10.1016/j.ceramint.2014.01.157]

[16] Altermatt, U.D.; Brown, I.D. A real-space computer-based symmetry algebra. *Acta Crystallogr. A,* **1987**, *34*, 125.
[http://dx.doi.org/10.1107/S0108767387099756]

[17] Liu, C.; Rondinone, A.J.; Zhang, Z.J. Synthesis of magnetic spinel ferrite $CoFe_2O_4$ nanoparticles from ferric salt and characterization of the size-dependent superparamagnetic properties. *Pure Appl. Chem.,* **2000**, *72*, 37-45.
[http://dx.doi.org/10.1351/pac200072010037]

[18] Labde, B.; Sable, M.C.; Shamkuwar, N. Structural and infra-red studies of $Ni_{1+x}Pb_xFe_{2-2x}O_4$ system. *Mater. Lett.,* **2003**, *57*, 1651-1655.
[http://dx.doi.org/10.1016/S0167-577X(02)01046-7]

[19] Waldron, R.D. Infrared spectra of ferrites. *Phys. Rev.,* **1955**, *99*, 1727-1735.
[http://dx.doi.org/10.1103/PhysRev.99.1727]

[20] Sanpo, N.; Berndt, C.C.; Wen, C.; Wang, J. Transition metal-substituted cobalt ferrite nanoparticles for biomedical applications. *Acta Biomater.,* **2013**, *9*(3), 5830-5837.
[http://dx.doi.org/10.1016/j.actbio.2012.10.037] [PMID: 23137676]

[21] Dhiman, M.; Singhal, S. Enhanced catalytic properties of rare-earth substituted cobalt ferritesfabricated by sol-gel auto-combustion route. *Mater. Today: Proceedings,* **2019**, *14*, 435-444.

[22] Macdonald, J.R. *Impedance Spectroscopy-Emphasizing Solid Materials and Synthesis,* 3rd ed; Wiley: New York, **1987**.

[23] Belam, W.; Essoumhi, A.; Satre, P. Synthesis and Physico-Chemical Characterizations of the Lithium-Substituted NASICONS Series with General Formula $Li_{2.8}Zr_{2-y}Si_{1.8-4y}P_{1.2+4y}O_{12}$ where ($0 \leq y \leq 0.45$). *Z. Phys. Chem.,* **2007**, *221*, 225-234.
[http://dx.doi.org/10.1524/zpch.2007.221.2.225]

[24] Mechergui, J.; Belam, W. Synthesis, structure refinement at 296 K and physico-chemical characterizations of $KMnHP_3O_{10}$. *Mater. Res. Bull.,* **2007**, *43*, 3358-3367.
[http://dx.doi.org/10.1016/j.materresbull.2008.02.018]

[25] Belam, W.; Mechergui, J. Synthesis, X-ray diffraction study and physico-chemical characterizations of $KLaP_4O_{12}$. *Mater. Res. Bull.,* **2008**, *43*, 2308-2317.
[http://dx.doi.org/10.1016/j.materresbull.2007.08.021]

[26] Belam, W. Elaboration and physico-chemical characterizations of the series of nanomaterials: Lithium-substituted NASICONS with general formula $Li_{3.2}Zr_{2-y}Si_{2.2-4y}P_{0.8+4y}O_{12}$ where ($0 \leq y \leq 0.55$). *Z. Phys. Chem.,* **2009**, *223*, 319-328.
[http://dx.doi.org/10.1524/zpch.2009.5437]

[27] Belam, W. Sol–gel chemistry synthesis and DTA–TGA, XRPD, SIC and ^{7}Li, ^{31}P, ^{29}Si MAS–NMR studies on the Li-NASICON $Li_3Zr_{2-y}Si_{2-4y}P_{1+4y}O_{12}$ ($0 \square y \square 0.5$) system. *J. Alloys Compd.,* **2013**, *551*, 267-273.
[http://dx.doi.org/10.1016/j.jallcom.2012.10.005]

[28] Jonscher, A.K. The 'universal' dielectric response. *Nature,* **1977**, *267*, 267-679.
[http://dx.doi.org/10.1038/267673a0]

[29] Andoulsi, R.; Horchani-Naifer, K.; Férid, M. Structural and electrical properties of calcium substituted lanthanum ferrite powders. *Powder Technol.,* **2012**, *230*, 183-187.
[http://dx.doi.org/10.1016/j.powtec.2012.07.026]

[30] Vijaya Bhasker Reddy, P.; Ramesh, B.; Gopal Reddy, Ch. Electrical conductivity and dielectric properties of zinc substituted lithium ferrites prepared by sol-gel method. *Physica B,* **2010**, *405*, 1852-1856.
[http://dx.doi.org/10.1016/j.physb.2010.01.062]

[31] Belam, W. Sol-gel chemistry autocombustion synthesis and physicochemical characterizations of the series of Li–Cu cobalt ferrite nanoparticles $LiCu_{(1-2Y)}Co_{(1-Y)}Fe_{(1+2Y)}O_4$. *J. Mol. Struct.,* **2020**, *1209*127937
[http://dx.doi.org/10.1016/j.molstruc.2020.127937]

[32] Jacob, J.; Khader, M. Investigation of mixed spinel structure of nanostructured nickel ferrite. *J. Appl. Phys.,* **2010**, *107*, 114310-114320.
[http://dx.doi.org/10.1063/1.3429202]

[33] Singh, M.; Ulbrich, P.; Prokopec, V.; Svoboda, P.; Santava, E.; Stepanek, F. Vapour phase approach for iron oxide nanoparticle synthesis from solid precursors. *J. Solid State Chem.,* **2013**, *200*, 150-156.
[http://dx.doi.org/10.1016/j.jssc.2013.01.037]

[34] Thampi, A.; Babu, K.; Verma, S. Large scale solvothermal synthesis and a strategy to obtain stable Langmuir–Blodgett film of $CoFe_2O_4$ nanoparticles. *J. Alloys Compd.,* **2013**, *564*, 143-150.
[http://dx.doi.org/10.1016/j.jallcom.2013.02.139]

[35] Ribeiro, A.L. Characterization of soft magnetic materials using a modified Stoner-Wohlfarth model. *J. Magn. Magn. Mater.,* **1994**, *133*, 97-100.
[http://dx.doi.org/10.1016/0304-8853(94)90499-5]

[36] Neel, L. Propriétés magnétiques des ferrites: ferrimagnétisme et antiferromagnétisme. *Ann. Phys.,* **1948**, *3*, 137-198.
[http://dx.doi.org/10.1051/anphys/194812030137]

[37] Deraz, N.M. Size and crystallinity-dependent magnetic properties of copper ferrite nanoparticles. *J. Alloys Compd.,* **2010**, *501*, 317-325.
[http://dx.doi.org/10.1016/j.jallcom.2010.04.096]

[38] Néel, L. Théorie du traînage magnétique des ferromagnétiques en grains fins avec applications aux terres cuites. *Ann. Geophys.,* **1949**, *5*, 99-136.